



HAL
open science

Putative Methanogenic Biosphere in Enceladus's Deep Ocean: Biomass, Productivity, and Implications for Detection

Antonin Affholder, François Guyot, Boris Sauterey, Régis Ferrière, Stéphane Mazevet

► To cite this version:

Antonin Affholder, François Guyot, Boris Sauterey, Régis Ferrière, Stéphane Mazevet. Putative Methanogenic Biosphere in Enceladus's Deep Ocean: Biomass, Productivity, and Implications for Detection. *The Planetary Science Journal*, 2022, 3 (12), pp.270. 10.3847/PSJ/aca275 . hal-04031926

HAL Id: hal-04031926

<https://hal.science/hal-04031926>

Submitted on 17 Mar 2023

HAL is a multi-disciplinary open access archive for the deposit and dissemination of scientific research documents, whether they are published or not. The documents may come from teaching and research institutions in France or abroad, or from public or private research centers.

L'archive ouverte pluridisciplinaire **HAL**, est destinée au dépôt et à la diffusion de documents scientifiques de niveau recherche, publiés ou non, émanant des établissements d'enseignement et de recherche français ou étrangers, des laboratoires publics ou privés.



Distributed under a Creative Commons Attribution 4.0 International License



Putative Methanogenic Biosphere in Enceladus's Deep Ocean: Biomass, Productivity, and Implications for Detection

Antonin Affholder^{1,2,8} , François Guyot^{3,4}, Boris Sauterey^{1,2,9} , Régis Ferrière^{1,6,7,10} , and Stéphane Mazevet^{5,10} ¹ Institut de Biologie de l'École Normale Supérieure École Normale Supérieure, Université Paris Sciences et Lettres, 46 Rue d'Ulm, F-75005 Paris, France; antonin.affholder@bio.ens.psl.eu, aaffholder@arizona.edu² Institut de Mécanique Céleste et de Calcul des Éphémérides Observatoire de Paris, Université Paris Sciences et Lettres, 77 Avenue Denfert-Rochereau, F-75014 Paris, France³ Institut de Minéralogie, de Physique des Matériaux et de Cosmochimie Muséum National d'Histoire Naturelle, CNRS, Sorbonne Université Paris, France⁴ Institut Universitaire de France (IUF), France⁵ Observatoire de la Côte d'Azur, 96 Boulevard de l'Observatoire, F-06300 Nice, France⁶ International Research Laboratory for Interdisciplinary Global Environmental Studies (iGLOBES) CNRS, ENS, Université Paris Sciences et Lettres, University of Arizona, Tucson, AZ, USA⁷ Department of Ecology and Evolutionary Biology, University of Arizona, Tucson, AZ, USA

Received 2022 February 17; revised 2022 November 8; accepted 2022 November 9; published 2022 December 13

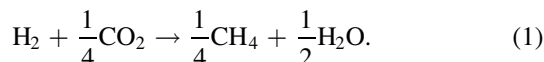
Abstract

Saturn's moon Enceladus is a top candidate in the search for extraterrestrial life in our solar system. Ecological thermodynamic modeling of the plume composition data collected by NASA's Cassini mission led to the hypothesis that a hydrogenotrophic methanogenic ecosystem might exist in the putative hydrothermal vents at Enceladus's seafloor. Here we extend this approach to quantify the ecosystem's expected biomass stock and production and evaluate its detectability from the collection of plume material. We find that although a hypothetical biosphere in Enceladus's ocean could be small (<10 tons of carbon), measurable amounts of cells and organics might enter the plume. However, it is critical that missions be designed to gain meaningful insights from a negative outcome (no detection). We show that in order to sample a cell from the plume with 95% confidence, >0.1 mL of material needs to be collected. This would require material from more than 100 fly-bys through the plume or using a lander. We then consider amino acid abundance as an alternative signature and find that the absolute abundance of amino acids, such as glycine, could be very informative if a detection threshold of $1 \times 10^{-7} \text{ mol L}^{-1}$ could be achieved. Altogether, our findings set relatively high bars on sample volume and amino acid detection thresholds, but these goals seem within the reach of near-future missions.

Unified Astronomy Thesaurus concepts: [Astrobiology \(74\)](#); [Saturnian satellites \(1427\)](#); [Planetary science \(1255\)](#); [Biosignatures \(2018\)](#)

1. Introduction

On Earth, hydrothermal circulation of seawater in the oceanic lithosphere triggers a set of reactions known as serpentinization that produces dihydrogen (H_2). H_2 molecules may then react with the seawater's carbon dioxide (CO_2) to produce methane (CH_4) according to the reaction equation (here written for 1 mol of H_2 , the electron donor):



This reaction can occur spontaneously (albeit slowly) in serpentinization fluids (McCollom 2016). Serpentinization fluids are released at seafloor hydrothermal vents, geological features known to harbor complex ecosystems that rely on chemical gradients instead of sunlight as their primary energy

source (Jannasch & Mottl 1985). In particular, reaction (1) can be enzymatically catalyzed by hydrogenotrophic, methanogenic archaea that use it as their catabolic reaction—the reaction that provides the cell with energy (Hedderich & Whitman 2013). Biological production of methane through reaction (1) is called methanogenesis.

Enceladus, the sixth-biggest moon of Saturn, might have similar hydrothermal vents in direct contact with its water ocean laying under a thick ice shell and over a rocky core (Iess et al. 2014; Hsu et al. 2015; Thomas et al. 2016). Warm buoyant water released at the seafloor rises upward, forming a rotating ocean plume that reaches the top of the water column (Goodman & Lenferink 2012; Choblet et al. 2017; Steel et al. 2017). Through cracks in the ice crust, oceanic material is outgassed and forms a plume of water vapor and ice grains (Spencer et al. 2013). Some of these particles contain salt and organic compounds, including high-mass molecules (macromolecules), suggesting that they are frozen droplets originating from gas bubbles bursting through an organic-rich film (Postberg et al. 2018). Bubble walls constitute an interface that attracts organics from the water table it traverses, thus increasing their concentration in the ocean spray (Walls et al. 2014). This process, known as bubble scrubbing, could occur during the formation of Enceladus's plume (Porco et al. 2017) as an important process in defining the effective composition of plume material relative to that of the bulk ocean or of the ocean plume.

⁸ Current address: Department of Ecology and Evolutionary Biology, University of Arizona, Tucson, AZ, USA.

⁹ Current address: Laboratoire d'Océanographie et du Climat: Expérimentations et Approches Numériques, Institut Pierre-Simon Laplace, Sorbonne Université/CNRS/IRD/MNHN, F-75005 Paris, France.

¹⁰ Co-senior authors.



While hydrothermal circulation in Enceladus's rocky core, unlike Earth's, is likely powered by tidal dissipation (Choblet et al. 2017), serpentinization might occur still (Waite et al. 2017). Previous work suggested that reaction (1) could be thermodynamically favored in Enceladus's ocean (Waite et al. 2017). It was also demonstrated that Earth's hydrogenotrophic methanogens could grow under putative Enceladus's seafloor conditions (Taubner et al. 2018) and that the observation of a H_2/CO_2 thermodynamical disequilibrium remains compatible with chemical energy consumption by methanogens (Hoehler 2022). Ecological thermodynamic modeling was used to quantitatively evaluate the habitability of Enceladus's hydrothermal vents for methanogens and estimate the likelihood of methanogenesis given H_2 and CH_4 abundances in the plume inferred from the Cassini data. The data appear to be compatible with sufficient H_2 production to allow a population of methanogens to grow and with production of CH_4 by abiotic serpentinization chemistry and a biotic population together, but as other abiotic sources of methane remain poorly constrained, this does not provide conclusive evidence in favor of living organisms (Affholder et al. 2021). To further investigate the possibility of a biological population in Enceladus's ocean, the critical challenges are to (i) predict biosignatures that would provide more direct evidence and be accessible to future missions and (ii) design such a mission so as to maximize scientific return, especially in the case of a negative result.

Previous work has focused on the concentrations of cells (Bedrossian et al. 2017; Porco et al. 2017) or organics (e.g., amino acids; Steel et al. 2017; Guzman et al. 2019) hypothetically present in the plume material and discussed how future missions could measure them. Here we build on the model presented in Affholder et al. (2021) to calculate the biomass stock and productivity of a hypothetical population of methanogens in Enceladus's ocean. In doing so, we are able to estimate cell densities and concentrations of biotically produced organics in a radially structured model of Enceladus's hydrothermal vent environment. We then can estimate the density of cells and organics in the initial ocean plume resulting from the buoyant hydrothermal fluid (HF)/seawater mix that composes the hydrothermal environment. The stock biomass that can be supported by Enceladus's hydrothermalism is not necessarily the same quantity as the biomass that can be found in the ocean plume. We therefore explicitly model the relationships between a population living in the hydrothermal vents and cells or organics that escape this environment and travel with buoyant water to the ice shell.

Our modeling approach relies on a description of biological energetic processes that ultimately govern the efficiency of hydrogen conversion by a population of methanogens, as well as on a spatial model of the hydrothermal environment and its chemical and temperature gradients. Thus, we expect our estimates of cell or biomass density to be more realistic—and more conservative—than those produced by models assuming complete conversion of H_2 into CH_4 (e.g., Bedrossian et al. 2017; Steel et al. 2017) or assuming constant catabolic energy yield for biomass generation (such as in Ray et al. 2021). Using this model, we obtain estimates of a priori credible amino acid and cell abundances in the plume under the assumption of methanogenesis, as well as estimates corresponding to a biomass stock and production best matching methane and dihydrogen measurements in the plume. In doing so, we show how previous data from the Cassini mission, as well as current

knowledge of serpentinization systems, can be used to formulate assumptions and models of Enceladus's hydrothermalism and provide quantitative, testable predictions. This could help design the experiments that could yield the best possible scientific return from a future mission to Enceladus.

2. Methods

The model presented here builds on the modeling and inference framework of Affholder et al. (2021) but focuses on quantities that were left out of their analysis such as biomass stock and biomass production. Indeed, Affholder et al. (2021) focused on the existence of a population and its effect on the local composition and ultimately on escape rates of volatile species in the plume, but they did not evaluate cell densities or ecosystem productivity.

2.1. Model of the Hydrothermal Environment

In Affholder et al. (2021), the hydrothermal environment is idealized as a single flat cylinder on the seafloor corresponding to a mixing layer (ML), in which HF is mixed with seawater. Given a total power dissipated hydrothermally of $F = 5$ GW (Choblet et al. 2017), the HF temperature T_f (in K, variable), and the ocean's temperature $T_o = 275$ K (Glein et al. 2015), steady-state physical quantities defining the hydrothermal environment are derived. $J_f(u)$ and $J_c(u)$ are, respectively, the surface advection flux in the environment (of HF) and the upward buoyancy flux coming out of the ML (both in $kg\ s^{-1}\ m^{-2}$) as a function of u , the distance to the center (meters). The expression of $J_c(u)$ is obtained by calculating the velocity of the water mass of temperature $T(u)$ at the top of the ML (height ϵ m) assuming that it has initial velocity of zero. This is done by integrating the expression of the temperature anomaly buoyancy acceleration (Equation (2) in Goodman et al. 2004):

$$J_c(u) = \rho \sqrt{2\epsilon g \alpha (T(u) - T_o)}, \quad (2)$$

where ρ ($1000\ kg\ m^{-3}$) is seawater mass density, α ($3 \times 10^{-4}\ K^{-1}$) is the coefficient of thermal expansion of water, and g ($0.12\ m\ s^{-2}$) is the local gravitational acceleration. Note that the unitary surface is removed from this equation for readability (see Equation (6) in Affholder et al. 2021). Strictly for numerical purposes, the thickness of the ML ϵ is assumed to be of the order of a meter (we set it to $\epsilon = 1$ m throughout), as it is intermediate between the height of the tallest spires in the Lost City Hydrothermal Field (LCHF; ≈ 60 m, Kelley et al. 2005) and the centimeter local scale of chimneys and ledges where archaea are present (Schrenk et al. 2004). In practice, the scale-free properties of the physical model imply that the value of ϵ or the assumption of a single vent instead of several has no influence on the quantities we calculate (see Appendix A).

The shape of function $J_f(u)$ ($kg\ s^{-1}\ m^{-2}$), the mass flux density of HF into the ML as a function of the distance, is assumed to be

$$J_f(u) = J_{\max} e^{-(u/c)^2} \quad (3)$$

and is governed by parameters J_{\max} (maximum flux, in $kg\ s^{-1}\ m^{-2}$) and c (horizontal scale, in m). In effect, c represents the distance from the center at which $J_f(c) = J_{\max}/e$, or equivalently $x^*(c) = e^{-2/3} \approx 0.5$ (the mixing

Table 1
Parameters of the Physical Model of the Hydrothermal Environment

Parameter	Value	Unit	Description	Reference
T_o	275	K	Ocean temperature	
g	0.12	m s^{-2}	Enceladus gravitational acceleration	Choblet et al. (2017)
F	$5 \cdot 10^9$	W	Hydrothermal vent heat dissipation power	Choblet et al. (2017)
ϵ	1	m	ML thickness	
C_p	4200	$\text{J K}^{-1} \text{kg}^{-1}$	Specific heat capacity of liquid water	
α	3×10^{-4}	K^{-1}	Thermal expansion coefficient for liquid water	
ρ_o	1000	kg m^{-3}	Seawater mass density	

Note. Adapted from Affholder et al. (2021).

Table 2

Range for the Concentrations and the Temperature of the Hydrothermal Fluid and the Concentrations in the Ocean (Ocean Temperature Is Fixed at $T_o = 275$ K) That Were Used in Simulations

Parameter	Distribution	Unit	Meaning
$[\text{H}_2]_f$	$\log_e U(10^{-8}, 10^{-1})$	mol kg^{-1}	Concentration of H_2 in the HF
$[\text{H}_2]_o$	$\log_e U(10^{-8}, 10^{-6})$	mol kg^{-1}	Concentration of H_2 in the ocean
$[\text{CH}_4]_f$	$\log_e U(10^{-8}, 10^{-4})$	mol kg^{-1}	Concentration of CH_4 in the HF
$[\text{CH}_4]_f'$	$\log_e U(10^{-8}, 10^{-1})$	mol kg^{-1}	Concentration of CH_4 in the HF (alternate scenario)
$[\text{CH}_4]_o$	$\log_e U(10^{-8}, 10^{-6})$	mol kg^{-1}	Concentration of CH_4 in the ocean
$[\text{DIC}]_f$	$\log_e U(4 \times 10^{-8}, 10^{-6})$	mol kg^{-1}	Dissolved carbon concentration in the HF
$[\text{DIC}]_o$	$\log_e U(4 \times 10^{-3}, 10^{-1})$	mol kg^{-1}	Dissolved carbon concentration in the ocean
T_f	$U(320, 600)$	K	HF temperature
F_{Gly}	$\log_{10} U(0.19, 10.44)$	g s^{-1}	Abiotic glycine production in the HF

Note. These ranges are taken from Affholder et al. (2021). U denotes the uniform distribution.

ratio at this distance is 1:1 HF vs. seawater). Keeping in mind that this model is an idealized representation of the hydrothermal environment, this scale would be ≈ 8 m for a 5 GW vent releasing 353 K fluid (or about 2 cm for a 40 kW, 353 K vent, the predicted output from the LCHF; Lowell 2017). They are obtained by ensuring that power F is dissipated by the advection of HF and by setting $J_f(0) = J_{\text{max}} = J_{c|T(u)=T_f}$:

$$\int_S J_f dS = \int_0^\infty 2\pi r J_f(u) du = \frac{F}{C_p(T_f - T_o)}, \quad (4)$$

where S (m^2) is the hot spot surface area, and hence

$$c^2 = \frac{F}{\pi C_p \rho \sqrt{\epsilon g \alpha} (T_f - T_o)^3}, \quad (5)$$

where C_p is the specific heat capacity of water ($4200 \text{ J K}^{-1} \text{ kg}^{-1}$).

Given the chemical composition of the HF and of the seawater, the steady-state composition in the ML $\{C_i(u)\}$ (concentration of molecule i in mol kg^{-1}) is also obtained. Together, the physical and chemical gradients surrounding the hydrothermal vent define the environment in which a population of methanogens may grow. A population of methanogens changes the steady-state composition of the ML as explained in Affholder et al. (2021) and summarized below. The flux of i coming from the hydrothermal environment is then given by

$$\Phi_i = \int_0^\infty J_c(u) C_i(u) 2\pi u du. \quad (6)$$

The concentration of i at the base of the ocean plume, assuming that buoyant ML water mixes together, is

$$C_i^{\text{OP}} = \frac{\int_0^\infty J_c(u) C_i(u) 2\pi u du}{\int_0^\infty J_c(u) 2\pi u du}. \quad (7)$$

It is interesting to note that in Affholder et al. (2021) assumptions that constrain $J_c(u)$, the flux of HF in the ML, lead to an HF-to-seawater mixing ratio in the initial ocean plume that is independent of the vent's scale and of the HF's temperature and equals 1/3 (proof is obtained by expressing the stationary-state mixing ratio in the initial plume: $x_{\text{OP}}^* = \int x J_c / \int J_c$; see Appendix A). This HF-to-seawater ratio for the initial ocean plume, just above the ML, sets a benchmark comparison to the total HF-to-seawater dilution of 1:10 numerically estimated in Steel et al. (2017). All parameter values in the physical model are listed in Tables 1 and 2.

2.2. Stationary Biomass of a Methanogenic Population

Our biological model assumes that a minimal amount of energy is required to sustain cellular integrity and function, called the maintenance energy, and that the energy yield of the catabolic reaction varies as the population alters the composition of the medium. This second point is relevant to the assumption that a putative Enceladean methanogenic biosphere might be limited by the energy yield of the catabolic reaction more than by electron donor availability. This assumption might be particularly relevant in the context of chemo-litho-autotrophs such as the hydrogenotrophs described here because the catabolic reaction yields low amounts of energy compared

Table 3
Parameters of the Biological Model

Parameter	Value	Unit	Description	Reference
$\Delta_r G_{S,cat}^0$	-32.6	kJ mol^{-1}	Standard Gibbs energy of the catabolic reaction	
$\Delta_r H_{S,cat}^0$	-63.2	kJ mol^{-1}	Standard enthalpy of the catabolic reaction	
$e_m(T)$	$84 e^{\frac{69,400}{R}(\frac{1}{298} - \frac{1}{T})}$	$\text{kJ day}^{-1} \text{mol}_C^{-1}$	Specific cell maintenance energy	Tijhuis et al. (1993)
ΔG_{diss}	1088	kJ mol_C^{-1}	Required energy dissipation for biomass synthesis	Affholder et al. (2021)
T_{eq}	90	$^{\circ}\text{C}$	Temperature at which activated and inactivated enzymes are in equal quantity	Daniel et al. (2010)
$\Delta G_{a,cat}$	72	kJ mol^{-1}	Activation energy of the catabolic reaction	Daniel et al. (2010)
ΔH_{eq}	305	kJ mol^{-1}	Equilibrium enthalpy of enzyme deactivation	Daniel et al. (2010)
τ	1.73×10^{-5}	dimensionless	Ratio of catabolic enzymes to biomass	Affholder et al. (2021)
d	0.03	day^{-1}	Baseline cell death rate	Connolly & Coffin (1995)

Note. Adapted from Affholder et al. (2021).

to most other catabolisms (Kleerebezem & Van Loosdrecht 2010). It thus seems important to couple cellular and population dynamics with energy yield changes using the Nernst equation (Equation (13); see also Higgins & Cockell 2020).

As our model only considers energy provided by the catabolic reaction as the resource consumed by the population, it amounts to assuming that the viability (initial growth rate) and the biomass production and stock are limited by the catabolic energy yield rather than nutrient availability. It is not currently known whether autotrophic production in hydrothermal vents is energy or nutrient limited, and it is not straightforward to find out. Autotrophic methanogenic archaea can fix nitrogen if deprived of bioavailable NH_4^+ and are thus unlikely to be limited by nitrogen availability in Earth's ecosystems where N_2 is abundant (DeMoll 1993). In Earth's natural settings where methanogens are found, H_2 is observed to be consumed rapidly, even if present at low concentrations (Wolin 1976), suggesting that H_2 rather than anabolic nutrients may be limiting, which is consistent with the catabolic energy yield being limiting. Moreover, it is likely that NH_4^+ and phosphorus are both present in Enceladus's ocean, thus making it less likely that the growth of methanogens be limited by either of these nutrients (Cable et al. 2021; Hao et al. 2022).

Methanogens catalyze reaction (1) yielding the specific catabolic rate q_{cat} (s^{-1}) and use the Gibbs free energy associated with it (noted ΔG_{cat}) to fuel their metabolism. In particular, cells need to fulfill their specific maintenance requirements e_m ($\text{J mol}^{-1} \text{s}^{-1}$; see expression in Table 3) in order to allocate energy to growth. The model by Affholder et al. (2021) assumes cell internal steady state (between growth and division), which allows one to focus on bulk biomass while ignoring cell density and bypassing the need for a specific relationship between a cell's internal biomass and division rate. Such a relationship needs to be modeled in order to derive cell density in addition to biomass concentration. Sauterey et al. (2020) proposed the following expression for the division rate r (s^{-1}) as a function of internal biomass B_c (in moles of carbon, mol_C):

$$\begin{cases} r(B_c) = \frac{1}{60 \times 60 \times 24} \frac{r_{max}}{1 + ((B_c - 2B_{struct})/B_{struct})^{-\theta}} & \text{if } B_c > 2B_{struct} \\ r(B_c) = 0 & \text{otherwise.} \end{cases} \quad (8)$$

where $r_{max} = 50 \text{ day}^{-1}$ (hence the conversion to seconds) is the theoretical maximum initial growth rate (the model hyperthermophilic methanogen *Methanococcus jannaschii* was observed

dividing up to 55 times a day in optimal conditions; Jones et al. 1983), $\theta = 10$, and B_{struct} is a minimal quantity of biomolecules (in carbon moles) the cell needs in order to divide. This quantity is derived from the cell's volume V (in μm^3) through (Menden-Deuer & Lessard 2000; Ward et al. 2012)

$$B_{struct} = 1.8 \times 10^{-14} V^{0.94}. \quad (9)$$

This empirical law is a power law of cell volume (of the form aV^b) commonly used in ocean ecosystem modeling for diverse biological parameters and rates (Ward et al. 2012), and it was also used in Sauterey et al. (2020) for modeling the Archean Earth's biosphere. The parameters of this power law were found in Menden-Deuer & Lessard (2000). Here we assume that cells are spheres of $1 \mu\text{m}$ radius (which is the typical scale for methanogenic archaea; e.g., Oren 2014). As a result, $B_{struct} \approx 6.92 \times 10^{-14} \text{ mol}_C$, or about $8.30 \times 10^{-13} \text{ gC}$.

Change in the cell's internal biomass follows

$$\frac{dB_c}{dt} = (q_{ana} - r(B_c))B_c, \quad (10)$$

where q_{ana} is the specific anabolic rate (s^{-1}), the rate at which biomolecules are produced in the cell. Assuming internal steady state (B_c^* such that $dB_c/dt = 0$) yields

$$q_{ana} = r(B_c^*), \quad (11)$$

hence the following equation for the bulk biomass concentration $B = NB_c^*$ (mol L^{-1} , with N the cell density in L^{-1}):

$$\frac{dB}{dt} = (q_{ana} - d)B, \quad (12)$$

where $d = 0.03 \text{ day}^{-1}$ is a constant, density-independent death rate (Connolly & Coffin 1995; Affholder et al. 2021). Parameter q_{ana} is computed from the catabolic energy yield $\lambda = -\Delta G_{cat}/\Delta G_{diss}$, where $\Delta G_{diss} \approx 1000 \text{ kJ mol}^{-1}$ is the energetic cost of building 1 mol of biomass (formally, this term is usually separated into a dissipation term and the negligible biosynthesis Gibbs free energy ΔG_{ana} ; Affholder et al. 2021) and

$$\Delta G_{cat} = \Delta G_{cat}^0 + RT \ln Q, \quad (13)$$

with ΔG_{cat}^0 the standard Gibbs free energy of the catabolic reaction, $R = 8.314 \text{ J K}^{-1} \text{ mol}^{-1}$ the ideal gas constant, T the temperature (K), and Q the reaction quotient. For reaction (1), by approximating activities of chemical species with their

aqueous concentrations (denoted by the square brackets), we obtain

$$Q = \frac{[\text{CH}_4]^{0.25}}{[\text{H}_2][\text{CO}_2]^{0.25}}. \quad (14)$$

The standard Gibbs free energy is approximated by

$$\Delta_r G_{\text{cat}}^0(T) = \Delta_r G_{S,\text{cat}}^0 \frac{T}{T_S} + \Delta_r H_{S,\text{cat}}^0 \frac{T_S - T}{T_S}, \quad (15)$$

where $\Delta_r G_{S,\text{cat}}^0 = -32.6 \text{ kJ mol}^{-1}$ and $\Delta_r H_{S,\text{cat}}^0 = -63.2 \text{ kJ mol}^{-1}$ are, respectively, the standard Gibbs free energy and standard enthalpy of the catabolic reaction at $T_S = 298 \text{ K}$. q_{ana} also depends on temperature-sensitive kinetic parameters described in Affholder et al. (2021) and recalled here:

$$q_{\text{ana}} = \lambda q_{\text{cat}} - q_m, \quad (16)$$

where $q_m = e_m/\Delta G_{\text{diss}}$ (s^{-1}) and q_{cat} (s^{-1}) is the enzymatically accelerated rate of the catabolic reaction, calculated using enzymatic rate modeling as in Daniel et al. (2010),

$$\begin{aligned} q_{\text{cat}} &= \tau q_e \\ q_e &= \frac{k_{\text{cat}}}{1 + K_{\text{eq}}} \\ k_{\text{cat}} &= \frac{k_B}{h} T e^{-\frac{\Delta G_{a,\text{cat}}}{RT}} \\ K_{\text{eq}} &= e^{-\frac{\Delta H_{\text{eq}}}{R} \left(\frac{1}{T_{\text{eq}}} - \frac{1}{T} \right)}, \end{aligned} \quad (17)$$

where $k_B = 1.38 \times 10^{-23} \text{ J K}^{-1}$ is the Boltzmann constant and $h = 6.63 \times 10^{-34} \text{ J s}$ is the Planck constant. The meaning, values, and units of τ , $\Delta G_{a,\text{cat}}$, ΔH_{eq} , and T_{eq} are given in Table 3. Note that we introduce a slight change in notation compared to Affholder et al. (2021), as they defined $q_m = -e_m/\Delta G_{\text{cat}}$, which is the threshold catabolic rate (the catabolic rate required to compensate maintenance loss) and not the maintenance rate per se. The catabolic rate couples biomass dynamics with the medium's composition according to

$$\frac{dC_i}{dt} = \frac{1}{\epsilon \rho} (J_f(C_f^i - C_o^i) + J_c(C_o^i - C_i)) + Y_i q_{\text{cat}} B, \quad (18)$$

where C_i^o and C_i^f are the concentrations of i in the ocean and the HF, respectively (Equation (19) in Affholder et al. 2021) and Y_i is the stoichiometric coefficient of molecule i in the catabolic reaction (e.g., $Y_{\text{H}_2} = -1$). Ultimately Equation (18) is solved to calculate C_i^{OP} , the concentration of i in the initial ocean plume according to Equation (7). The biological model and temperature alone set the steady-state ($q_{\text{ana}} = d$ in Equation (12)) value of the catabolic reaction free energy, obtained from Equation (16),

$$\Delta G_{\text{cat}}^*(T) = -\frac{\Delta G_{\text{diss}}}{q_{\text{cat}}(T)}(d + q_m), \quad (19)$$

which has its highest value (lowest energy limitation) at the optimal growth temperature $T_{\text{opt}} \approx 77^\circ\text{C}$, $\Delta G_{\text{cat}}^*(T_{\text{opt}}) \approx -23 \text{ kJ mol}^{-1}$. In other words, growth can occur only if $\Delta G_{\text{cat}}(T) \leq \Delta G_{\text{cat}}^*(T) \leq -23 \text{ kJ mol}^{-1}$ and at the steady state of the microbial population, $\Delta G_{\text{cat}}(T) = \Delta G_{\text{cat}}^*(T)$. This limit value of $\Delta G_{\text{cat}}^*(T_{\text{opt}})$ is slightly lower (and thus more conservative) than estimates of the minimally required

catabolic energy yield summarized in Hoehler (2004), which typically stand in the -10 to -20 kJ mol^{-1} range.

We use Equations (13), (14), and (19) to express the value of the steady-state reaction quotient Q^* . Then, Equation (22) in Affholder et al. (2021) allows us to rewrite Equation (14) and solve numerically a system of three equations, one for each reactant and product in Equation (1), to obtain the steady-state concentrations of molecules involved in the catabolic reaction C_i^* . Ultimately, Equation (18) equal to zero is solved for the steady-state values of bulk biomass concentration B^* . Using Equation (8), combined with Equations (11) and (16), allows the derivation of the steady-state cell density $N^* = B^*/B_c^*$, where B_c^* is obtained by solving Equation (8) at the steady state of the population (Equation (12) equal to zero):

$$B_c^* = B_{\text{struct}} \left(\left(\frac{r_{\text{max}}}{d} - 1 \right)^{-\frac{1}{\theta}} + 2 \right). \quad (20)$$

Note that with $\theta = 10$, B_c^* (and thus N^*) is weakly dependent on r_{max} (10% change when r_{max} is changed from 1 to 100). Thus, B_c^* to the first order depends on the empirically derived B_{struct} .

The total biomass or number of cells in the Enceladean hydrothermal environment is then obtained by integrating B^* and N^* over the volume of the ML:

$$\begin{cases} N_{\text{tot}} = \rho \epsilon \int N^*(u) 2\pi u du \\ B_{\text{tot}} = \rho \epsilon \int B^*(u) 2\pi u du. \end{cases} \quad (21)$$

2.3. Productivity of a Population of Methanogens

The productivity of the system is defined as the production of biomass when the system is at steady state. By definition, the productivity at steady state is equal to the total mortality. It is the quantity of biomass that leaves the stock of living cells per unit of time. It includes ‘‘waste’’ molecules corresponding to the maintenance loss term, but also the biomass in cells that die. Here the biomass mortality is equal to the constant death rate plus the maintenance term e_m defined in Equation (16). Thus, combining Equations (12) and (16), the specific productivity P_B ($\text{mol}_C \text{ s}^{-1} \text{ mol}_C^{-1}$) is given by

$$P_B = \left(\frac{e_m}{\Delta G_{\text{diss}}} + d \right). \quad (22)$$

Consequently, the productivity of the population at steady state is $P_B B^*$ integrated over the ML,

$$P_{B,\text{tot}} = \rho \epsilon \int P_B(u) B^*(u) 2\pi u du. \quad (23)$$

2.4. Dead Cells and Waste Biomass Densities in the Initial Plume

At steady state, the population does not stop dividing, but it replaces cells lost to mortality and waste (biomolecules that lost their function) through maintenance. Here we track two quantities: the number of dead cells produced by the stationary-state population and the productivity of the system. The former is simply the number of cells (dead cells, N_d , kg^{-1}) that may leave the localized environment (hydrothermal vent surroundings). This is equivalent to assuming that these

organisms live fixed in the ML (without assuming a specific fixation mechanism, which could be a biofilm; e.g., Brazelton et al. 2006). Thus, the derivative of the dead cells' concentration at a given location around the hydrothermal vent is

$$\frac{dN_d}{dt} = Nd - \frac{J_c}{\rho\epsilon} N_d \quad (24)$$

with steady state

$$N_d^* = \frac{\rho\epsilon}{J_c} N^* d, \quad (25)$$

where $\rho = 1000 \text{ kg m}^{-3}$ is the seawater density and $\epsilon = 1 \text{ m}$ is the ML thickness. In Appendix B, we show that the calculation of the steady-state concentration of cells that leave the ML is independent of the entrainment rate at which dead cells are detached from the biofilm (as long as it is not zero). Second, the productivity defined in Equation (22) can serve to estimate the total concentration of free-floating biomass in the ML (B_d , mol kg^{-1}) that is carried upward with buoyant water:

$$\frac{dB_d}{dt} = B^* P_B - \frac{J_c}{\rho\epsilon} B_d \quad (26)$$

with steady state

$$B_d^* = \frac{\rho\epsilon}{J_c} P_B B^*. \quad (27)$$

Ultimately, concentrations in the initial ocean plume are obtained by combining Equations (7), (25), and (27). As the ocean plume travels upward in the ocean and as oceanic material traverses the ice crust and is outgassed into space, its composition might be altered by additional dilution, bubble scrubbing, or other unknown processes. Here we assume as the baseline scenario that the concentrations of organics and cells in the plume are the same as in the initial ocean plume. This assumption is later discussed in Section 3.5.

2.5. Prior and Posterior Densities

2.5.1. Monte Carlo Sampling of Numerical Simulations

Prior densities are estimated by running 20,000 simulations with parameters (composition and temperature of the HF and ocean) randomly drawn from the distributions defined in Affholder et al. (2021) (these distributions are recalled in Table 2).

As the present study focuses on the detectability of a hypothetical biosphere, only 8763 simulations that produced habitable conditions were retained, and the distribution of their outputs (cell density, total biomass, glycine concentration) is referred to here as the prior density. Therefore, this distribution corresponds to the portion of the parameter space bounded by maximum concentrations of H_2 and CH_4 obtained in serpentinization experiments (e.g., McCollom & Donaldson 2016) and maximum fluid temperature estimated in Choblet et al. (2017) that allows a population to exist, regardless of its stock biomass and productivity. The posterior density is estimated from retaining the 1000 "biotic+abiotic" simulations (that are habitable and for which a population is simulated) that produced observables closest to Cassini observations (hydrogen and methane escape rate in the space plume reported in Waite et al. 2017), a standard method known as the k nearest neighbors (KNN; see Csilléry et al. 2010; Affholder et al. 2021, for details). Because the posterior

distribution is calculated only from biotic+abiotic simulations, this sets a stronger a priori constraint on the hydrogen escape rate Φ_{H_2} , which happens to match the latest estimates from Cassini measurements (Waite et al. 2017; Affholder et al. 2021), while the methane escape rate Φ_{CH_4} sets a stronger constraint a posteriori. In other words, the most determining factor for the goodness of fit of the biotic model was the escape rate of methane, although the assumption of the biotic model corresponds to an assumption on the hydrogen escape rate and thus remains contingent on the validity of the hydrogen abundance calculated in Waite et al. (2017). We find that the posterior distribution corresponds to the subset of the parameter space having methanogens that produce the largest amounts of methane, which thus matches the methane abundance measured in Waite et al. (2017), as shown in Affholder et al. (2021). Thus, the posterior distribution is also referred to as the methane-informed distribution. It is to be noted that this inference is based on the value of the fluxes of methane and dihydrogen in the plume instead of their concentration (Affholder et al. 2021). The underlying assumption is that the ocean is at steady state and that the escape rates of volatile molecules are equal to their production rates in the hydrothermal system. Hence, this inference is assumed to be insensitive to dilution (or concentration) processes that might affect the concentrations in the plume but not the fluxes. Because of that, the uncertainty in the prediction of the concentrations of cells or organics in the plume (see Section 3.5) is distinct from the uncertainty on Enceladus's ocean being at a steady state.

We first consider the distributions of simulated cell densities in the ocean plume, corresponding to dead cells escaping the system (Section 2.4). This first set of simulations uses model parameters sampled in the prior distributions shown in Table 2. These simulations can be used to conduct a prospective Bayesian inference, in which data that are not yet available (such as abundance of glycine in the plume) are used in the form of a variable to calculate posterior probabilities of the presence of Earth-like methanogens as a function of the value of this variable. In this context, the simulated glycine concentrations form a prior distribution. However, the escape rates of methane and dihydrogen are known (Waite et al. 2017) and have been used to constrain the habitability of Enceladus's hydrothermal vents (Affholder et al. 2021), which amounts to constraining the composition and temperature of the HF and seawater within the prior distributions shown in Table 2. Simulations that best match H_2 and CH_4 escape rates in the plume are also associated with a specific subset of simulated biomass production (and thus glycine concentration). In that sense, a posterior distribution with respect to the measure of Φ_{H_2} and Φ_{CH_4} also constitutes a prior distribution with respect to a hypothetical inference based on a measure of glycine abundance, for instance. Hence, we call prior distributions those where the parameters are sampled in Table 2 and posterior distributions those for which Φ_{H_2} and Φ_{CH_4} best match the observations, whereas Section 3.5 examines the posterior *confidence* in the existence of *biotic* glycine production (as opposed to only abiotic production) with respect to a hypothetical measure of the concentration of glycine in the plume.

A hypothetical measure falling outside of the interval should be interpreted as falsifying the biotic *and* abiotic models. Posterior probabilities relative to the measure of glycine

concentration in the plume (using a prior informed or not by the measure of volatile abundances by Cassini) are determined using Bayes's theorem

$$P(m|x^0) = \frac{P(x^0|m) \times P(m)}{P(x^0|m) \times P(m) + P(x^0|\bar{m}) \times P(\bar{m})}, \quad (28)$$

where m denotes a model or hypothesis (abiotic or abiotic +biotic, respectively noted A and B) and x^0 the observation. $P(x^0|m)$ is the probability (called the *likelihood*) of observing x^0 under model m , and $P(m)$ is the *prior* probability of m . \bar{m} denotes the complementary of m (i.e, theoretically *all other models*, here abiotic or biotic+abiotic accordingly).

Thus, the posterior probability of biotic+abiotic glycine production (model B) is

$$P(B|Gly = x^0) = \frac{P(Gly = x^0|B)P(B)P(H)}{P(Gly = x^0|B)P(B)P(H) + P(Gly = x^0|A)(1 - P(B)P(H))}, \quad (29)$$

where A denotes abiotic glycine production and H denotes habitability. Here the prior probability of B has been decomposed as

$$P(B) = P(B|H)P(H), \quad (30)$$

where $P(H)$ is constrained by evaluating the viability of the modeled population over the distribution of environmental parameters in Table 2 (Affholder et al. 2021).

For visualization and integration purposes, the simulated samples are used to perform a Gaussian kernel density estimate implemented in Python's *scipy* package (Virtanen et al. 2020), a standard method to approximate densities.

2.5.2. Determination of the Credible Interval

In this section, we determine the interval of the glycine concentration [Gly] values that are predicted by the models A (abiotic) or B (biotic+abiotic) with reasonable confidence, so as to exclude values that are predicted with low probability by either model from our analysis. Here we determine the interval space of glycine concentration that lies above a so that

$$\int_0^a P([Gly] = x|B)P(H)P(B|H) + P([Gly] = x|A) \times (1 - P(H)P(B|H))dx - 0.025 = 0 \quad (31)$$

and below b so that

$$\int_0^b P([Gly] = x|B)P(H)P(B|H) + P([Gly] = x|A) \times (1 - P(H)P(B|H))dx - 0.975 = 0. \quad (32)$$

In practice, we estimated densities for $\log_{10}[\text{Gly}]$ so that the lower numerical integration bound is $\log_{10}[\text{Gly}] = -10$, as probabilities of [Gly] being less than 10^{-10} mol kg⁻¹ are essentially equal to zero in our model. Equations (31) and (32) are solved numerically using the *Scipy* optimize package's *brentq* method (Virtanen et al. 2020).

2.6. Cell Detection False-negative Rate in a Sampling Mission

Here we estimate the probability that a mission sampling plume material fails to capture any cell even though a biosphere

is present in Enceladus's deep ocean. We transpose modeling of the probability to observe a cell in a sample in Bedrossian et al. (2017) to the probability that a sampling mission samples any cell at all. We argue that this sampling bottleneck is more relevant to estimating the limits to detecting a putative biosphere than estimating the chance that a cell is in the microscope's field of view, as samples can be concentrated (Bedrossian et al. 2017; Porco et al. 2017). Some instruments also require a minimum volume to function; thus, if the sample volume is lower than the requirement, it needs to be diluted (e.g., MacKenzie et al. 2021), in which case the sampling bottleneck is even more relevant.

The probability that no cell is present in the sample (negative result, denoted by \bar{N}) is given by

$$P(\bar{N}|\rho_b) = \left(1 - \frac{V}{V_{\text{tot}}}\right)^{\rho_b V_{\text{tot}}} \approx e^{-V\rho_b}, \quad (33)$$

where ρ_b is the cell density in the plume, V is the sampled volume, and V_{tot} is the total volume of the plume when the probe is sampling; thus, $V_{\text{tot}} \gg V$. Previous studies have estimated that a fly-by through Enceladus's plume could realistically collect a 1×10^{-4} mL sample (using a 0.04 m² collector plate for a fly-by at 50 km altitude; Porco et al. 2017). Bedrossian et al. (2017) and Porco et al. (2017) propose that several samples can be retrieved (across multiple fly-bys, or by passively collecting falling plume particles on the ice surface of Enceladus), as multiple mission concepts propose architecture offering this possibility (Cable et al. 2016; Eigenbrode et al. 2018; MacKenzie et al. 2021). We can thus rewrite Equation (33) in order to account for a number of fly-bys k_f that multiplies a unit volume V . Increasing the sampling effort thus lowers the probability of a false-negative result

$$P(\bar{N}|\rho_b, k_f) \approx e^{-k_f V \rho_b}. \quad (34)$$

Using the estimated probability density of dead cell density escaping the hydrothermal environment given by our biological and circulation model as ρ_b , we can estimate the overall false-negative risk, given only the sampling effort $k_f \times V$,

$$P(\bar{N}|k_f) = \int_{-\infty}^{\infty} P(N|\rho_b = z, k_f) \times P(\rho_b = z)dz. \quad (35)$$

Equivalently, the sample volume V can be kept as the variable, as the fly-by sampling events are assumed to be independent. The integral in Equation (35) is numerically approximated using Gaussian kernel approximation on simulated samples of the probability density of ρ_b .

As ρ_b corresponds to the concentration of cells in the space plume, and given that our model calculates N_d , the density of cells in the initial ocean plume, we define

$$\rho_b = N_d \times f_d, \quad (36)$$

with f_d being the dilution or concentration factor between densities in water directly above the hydrothermal vent and in the plume. This dilution (or concentration) factor is discussed further in Section 3.5.

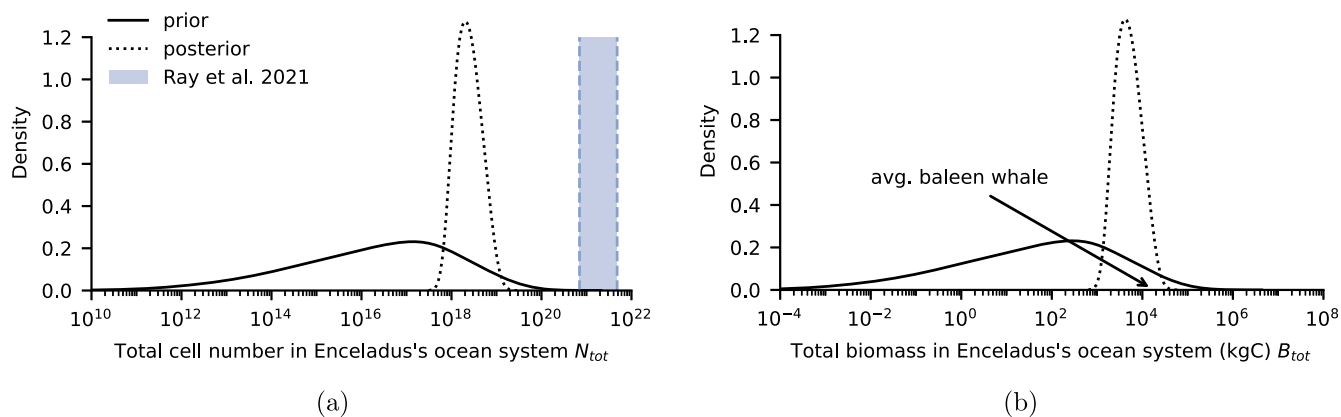


Figure 1. (a) Standing cell and (b) biomass population estimates. Dark curves are probability density estimates approximated from simulations using the equations in Section 2.2 and parameter values from Table 1. The black solid line uses the prior distributions in Table 2, and the dotted line uses the posterior distribution obtained by sampling simulations that best match escape rates of H_2 and CH_4 inferred from the Cassini data. The solid line represents the prior estimate, ignoring information from plume abundances of CH_4 and H_2 , while this information is used to refine the estimate for the dotted curve (posterior). The blue region in panel (a) represents the estimates of methanogenic cell abundance in Ray et al. (2021). In panel (b), the biomass of a single average baleen whale is given as an illustration and is taken from Pershing et al. (2010).

3. Results and Discussion

3.1. Estimates of the Total Biomass Supported by Hydrothermalism in Enceladus's Ocean

3.1.1. Cell Number Estimate

We simulate biomass and cell concentrations B^* and N^* (Section 2.2) under various conditions in the hydrothermal environment using distributions of HF composition and temperature described in Table 2. We also simulate biomass concentrations under the hypothesis that the methanogenic population produces the methane levels measured by the Cassini probe in the plume (Waite et al. 2017). In other words, we estimate (i) the standing biomass in Enceladus's hydrothermal environment that is possible given a range of assumptions for the HF's composition (referred to as the “prior” estimate) and (ii) the standing biomass that yields the best fit to the plume's composition (posterior). We find that our estimate of the total number of methanogenic cells N_{tot} (Equation (21)) supported by Enceladus's hydrothermalism (prior: $10^{16.26 \pm 3.01}$; posterior: $10^{18.38 \pm 0.07}$) is orders of magnitude lower than previously estimated (Figure 1(a)). Previous estimates assume either complete conversion of electron donor H_2 (Bedrossian et al. 2017; Steel et al. 2017) or that the catabolic yield is constant (that is, that the Gibbs free energy change associated with the catabolic reaction is constant) so that the number of cells at steady state is equal to the chemical energy flux (electron donor flux times catabolic Gibbs free energy) divided by the individual maintenance energy rate (Ray et al. 2021). We show that approaches describing the dynamic coupling between catabolic energy yield and cellular growth such as the one presented here and in Higgins & Cockell (2020) lead to more conservative estimates than electron-donor-limited approaches (such as Ray et al. 2021), which yield higher estimates. For instance, Figure 1(a) shows the comparison between the estimated number of cells of hydrogenotrophic methanogens estimated using the method in Ray et al. (2021) and the distribution of the simulations under our model, showing a difference of several orders of magnitude.

3.1.2. Standing Biomass Estimate

To better compare Enceladus's putative biosphere to Earth's, we estimate the total standing biomass B_{tot} (see details in Section 2.2, specifically Equations (18), (20), and (21)), measured in kilograms of carbon (kgC). We find that the simulated population of methanogens has a very low biomass (Figure 1(b)). In the prior case, the 95% confidence interval (CI) is $10^{1.57 \pm 3.07}$ kgC, or from negligible (less than 1 gC) to about 40 tC. In the methane-informed or posterior case, the CI is $10^{3.69 \pm 0.07}$ kgC or about 4–6 tC, about half the mass of carbon contained in a single typical baleen whale (Pershing et al. 2010). As a consequence, the methanogenic population that could be supported by a single 5 GW hydrothermal vent in Enceladus's ocean is very small in comparison to the size of Earth's ecosystems. In Appendix A, we show that modeling a single 5 GW vent or breaking it down in smaller vents feeding the same ocean plume is equivalent regarding all the quantities calculated by our model.

On Earth, most methanogenic archaea dwelling in hydrothermal vents are sessile (e.g., in microbial mats), and free-floating cells are due to entrainment by circulating fluid (Brazelton et al. 2006). Conservatively, we should assume that Enceladus's putative biosphere is also sessile and that the plume in space is not directly a sample of the habitable environment. As a consequence, if one is to estimate biomass or cell concentrations in the plume, other quantities than standing biomass have to be derived and integrated with a circulation model. Such other quantities should relate to the *production* term, which amounts to a loss term in the biomass stock, e.g., through death and subsequent entrainment.

3.2. Total Productivity of a Putative Methanogenic Biosphere

Primary production P_B (Equation (22)) measures the amount of biomass that an ecosystem or population synthesizes per unit time (usually in petagram or gigaton of carbon per year). At steady state, this quantity is by definition equal to the rate at which biomass escapes the considered system. Appendix B shows that adding an explicit entrainment term to the model is equivalent to equating the entrainment rate with the death rate in the population. In our model, the total productivity is orders

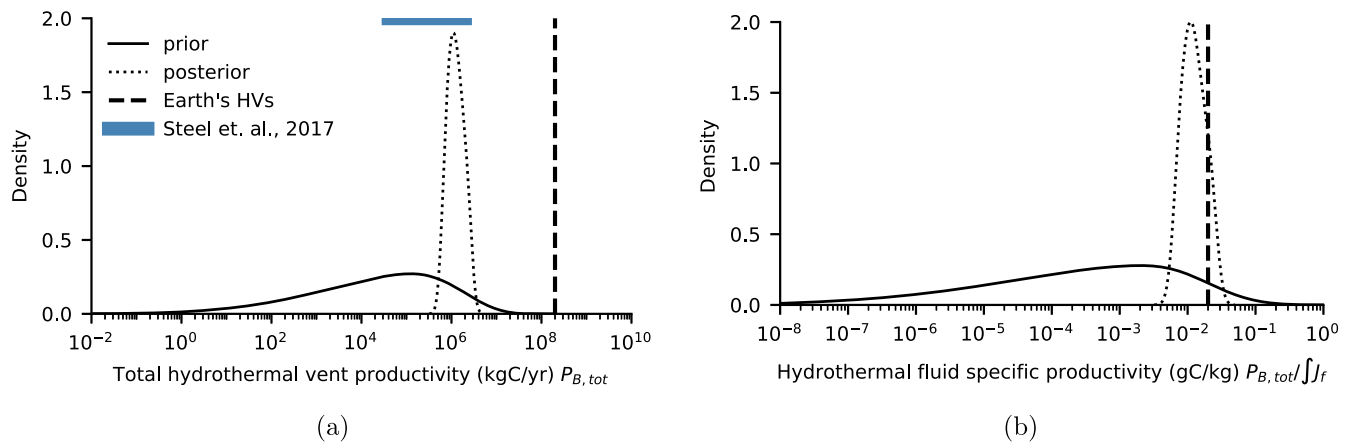


Figure 2. (a) Total hydrothermal vent productivity; (b) HF specific productivity. Dark curves are probability density estimates approximated from simulations using Equation (22) and parameter values from Table 1. The black solid curve uses the prior distributions in Table 2, and the dotted curve uses the posterior distribution obtained by sampling simulations that best match escape rates of H_2 and CH_4 observed by the Cassini mission. The vertical dotted line indicates an estimate of the biomass production in the HF and seawater mix around Earth’s hydrothermal vents obtained from computations in McCollom (2000).

of magnitude lower (2–4) than that of Earth’s hydrothermal vents (Figure 2(a)). Scaling with HF production, the simulated specific productivity of HF (the carbon mass of biomolecules that can be synthesized per kg of fluid) is close to the inference for Earth’s vents (McCollom 2000; Figure 2). This suggests that the difference of 2–4 orders of magnitude between the total productivity of Earth’s hydrothermal systems and that of Enceladus’s is mainly due to the difference in HF production, not in the composition or temperature of the produced HF. It is to be noted, however, that estimates of methanogenic primary production in Earth’s hydrothermal vent are poorly constrained, and to our knowledge only energy-based approaches as in McCollom (2000) have been used, and they have mostly been applied to global estimates for the deep biosphere rather than hydrothermal vents in particular (Bach & Edwards 2003; Orcutt et al. 2013). Therefore, the posterior distribution corresponds to an Earth-like hypothesis, at least for productivity. Affholder et al. (2021) only go as far as showing that there exists a subset of HF compositions within their prior that translates into biotic methane production matching with the observations. Here, however, we go into detailing what this subset of parameters corresponds to in terms of ecosystem productivity, and we show that it matches that of Earth’s hydrothermal vents ecosystems.

As detailed in Section 2, productivity (P_B , Equation (22)) is the relevant quantity to consider when estimating biomass and cells that leave the hydrothermal environment and that can be later found in the plume. Because of that, we now turn to the concentrations of (dead) cells and organics that would be found in the ocean plume if a population of Earth-like methanogens were to inhabit putative hydrothermal vents on Enceladus.

3.3. Densities of Cells in the Ocean Plume Predicted by the Model

Others have estimated possible methanogenic cell concentrations in different parts of Enceladus’s ocean using various models. For example, Steel et al. (2017) and Ray et al. (2021) estimate the flux of available Gibbs free energy in the HF and divide it by the energy required to form or sustain 1 mol of biomass assuming total conversion of H_2 . The authors then calculate the concentrations of cells in various volumes ranging from the plume to the whole ocean. Here, rather, we focus on

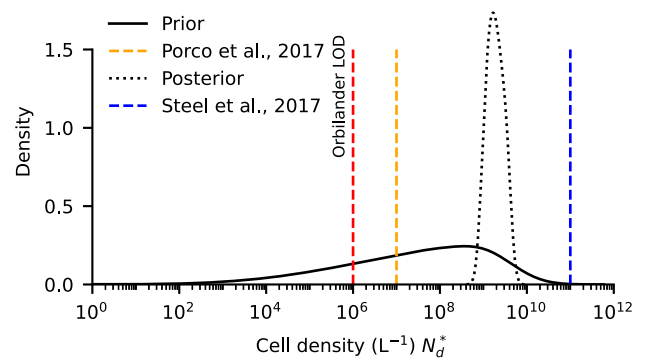


Figure 3. Cell densities in the ocean plume. The solid and dotted black curves are, respectively, the prior and posterior probability density estimates of dead cells’ concentration in water escaping the ML and composing the initial ocean plume. Our baseline assumption is that this sets the concentration throughout the ocean plume, as we assume all the dilution to occur in the ML. The orange dashed line corresponds to the estimate of plausible cell density in the plume from Porco et al. (2017). The blue dashed line represents the calculation in Steel et al. (2017) ($\approx 10^{11}$ cells kg^{-1}). The red dashed line highlights the limit of detection (LOD) assumed to design the Orbilander concept (MacKenzie et al. 2021) for reference.

the the fraction of ecosystem productivity corresponding to (dead or entrained) cells removed from the ML as the potential source for cells in the plume, N_d^* (Section 2.4, Equation (25)). While the productivity estimated in Steel et al. (2017) is in line with our estimates (Figure 2(a)), we estimate a much lower cell density in the plume (Figure 3) because we consider that the ocean plume is fed only by fossil organic matter.

Interestingly, our calculations of cell densities in the ocean plume are in most instances greater than estimates in Porco et al. (2017) (Figure 3). Their estimates are based on extrapolation (based on geothermal flux scaling) of cell densities in seawater around Earth’s hydrothermal vents (which include but are not limited to methanogens; Brazelton et al. 2006). On the other hand, calculations in Porco et al. (2017), which are based on energy dissipation scaling (as in Ray et al. 2021), yield higher estimates than our explicit ecosystem modeling. Hence, the empirical approach in Porco et al. (2017) might be viewed in that regard as most conservative. A key explanation for our model’s prediction of greater cell densities in the ocean plume could be that the death rate value used in

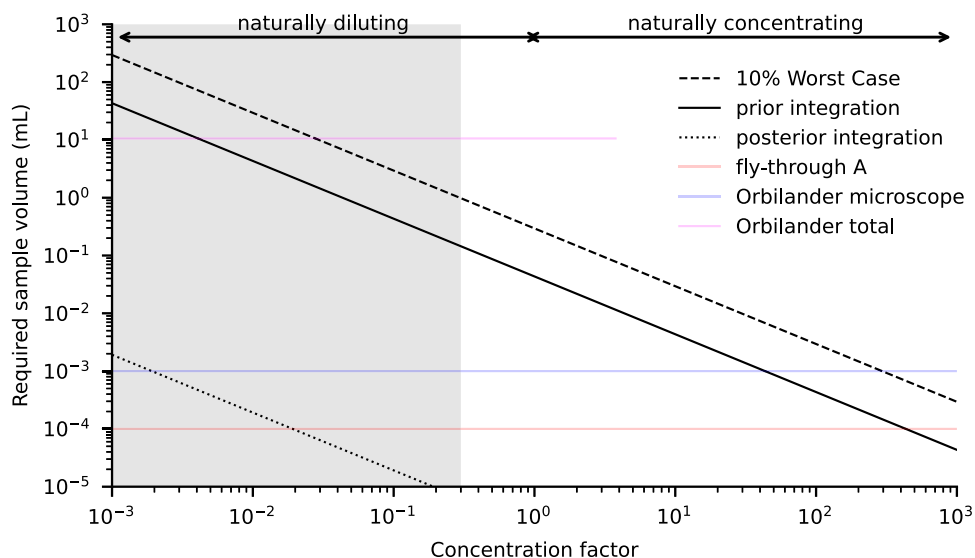


Figure 4. Required sample volume to capture at least one cell with 95% confidence as a function of the concentration factor. The concentration factor corresponds to a multiplicative term that either lowers (concentration factor <1) cell concentration in the space plume relative to the initial ocean plume (e.g., plume dilution, cell destruction) or concentrates (concentration factor >1) cells in the space plume relative to the initial ocean plume (e.g., bubble scrubbing). The dashed line corresponds to the required sample volume to get at least 1 cell with 95% probability assuming a cell density equal to the mean of the 10% simulations with the lower cell density. The solid (dotted) line represents this minimal sample volume assuming the prior (posterior) integrated probability density for the dead cell density in the plume. HF-to-seawater ratios lower than 1:10 are shaded gray, as they are deemed unlikely in Porco et al. (2017) and Steel et al. (2017). The horizontal red line denotes the sample volume collected from a 50 km altitude flight through the plume on a 0.04 m^2 collector plate as estimated in Porco et al. (2017). The blue line represents the required sample size proposed for the Orbilander microscope (Exhibit B-6 in MacKenzie et al. 2021). The magenta line denotes the total sample volume for the Orbilander concept (MacKenzie et al. 2021).

our model (Section 2.2), which serves as a basis to derive the dead cell densities in the plume, is poorly constrained for methanogens. We used a value that fits marine plankton (3% mortality per day; Table 1; Connolly & Coffin 1995) and that may or may not be greater than the actual basal component of the death rate of methanogens that could relate to cell entrainment. Nevertheless, we hold our simulations of cell densities as plausible, as they span from much below the relatively conservative calculation of Porco et al. (2017) to slightly less than the optimistic value in Steel et al. (2017).

While estimates of cell concentrations in the ocean plume in Steel et al. (2017) and Porco et al. (2017) fall above detection threshold values that have been previously proposed (Bedrossian et al. 2017; MacKenzie et al. 2021), we find that a small but nonnegligible portion of our prior distribution falls below this threshold (Figure 3). Modeling the uncertainty of Enceladus's putative HF composition as prior distributions allows us to calculate not a single point estimate but a distribution of what could be possible. Doing so allows us to bound the risk of a false negative: when no cells are detected despite a biosphere existing in the ocean. We thus propose constraints on the sampling effort in the space plume required to capture cells with sufficiently high confidence.

3.4. Sampling Effort Required for the Capture of Cells in Plume Material

Evaluating the risk of a false negative (i.e., the probability that an experiment gives a negative result even though the tested condition is true) can help inform instrument design so that the interpretation of negative results becomes easier. Indeed, obtaining a negative result when efforts have been made to reduce the risk of a false negative provides a stronger argument to discard the hypothesis, here that methanogens are present in Enceladus's deep ocean. There are various sources of

false-negative or false-positive error about the detection of a cell in a sample, which can depend on the detection method. For example, Archean paleontologists are confronted with the existence of abiotic organic biomorphs exhibiting microfossil-like signatures (Criouet et al. 2021).

Assuming that there exists a method that enables us to detect even a single cell in a sample of plume material—whether in situ or by means of a sample return mission (Tsou et al. 2012; Nadeau et al. 2016; Neveu et al. 2020)—what are the chances that a single cell or more are sampled? Small sample sizes can result in sampling bias, altering the effective cell density in the sample relative to that in the plume. In some cases even, this sampling bias can result in no cell at all being sampled from the plume, even in the case in which plume material contains cells. We are interested here in constraining the minimal sample size required to obtain at least one cell with 95% confidence or more, in other words, to bring the risk of sampling zero of the cells present in the plume under 5%.

Using Equation (34), we compute the false-negative risk as a function of sampling volume (Figure 4). Because processes altering the composition of the plume relative to that of the ocean plume at the bottom of the ice shell are poorly constrained, we account for dilution up to a factor 1:1000 and for concentration enhancement by bubble scrubbing up to a factor 1000 (Figure 4) by multiplying N_d^* (Equation (25)) by 0.001–1000. First, we look at two fly-by collected sample sizes studied in Porco et al. (2017; fly-through A, 0.04 m^2 plate at 50 km altitude, resulting in a $\approx 10^{-4}$ mL sample) and Guzman et al. (2019; fly-through B, 1 m^2 plate at 25 km altitude, resulting in a $\approx 10^{-3}$ mL sample). Both sample sizes result in cell detection false-negative risks greater than 5% in the uninformed case (prior) unless we assume some amount of bubble scrubbing: at least a 20-fold concentration increase for sample B and by a few hundreds for sample A. To reach acceptable probabilities of sampling a cell without relying on

bubble scrubbing and in the uninformed case, the volume that has to be sampled should be at least 0.1 mL, or about 100 low plume fly-throughs with the larger plate.

While this number of plume fly-throughs may seem high, a comparable or greater order of magnitude (up to 1000 plume fly-throughs) is envisioned for the Enceladus Orbilander mission concept (MacKenzie et al. 2021). Alternative or complementary strategies have been proposed, including passive or active collection of plume material that has fallen on Enceladus's surface by a landed component as assessed by Porco et al. (2017) and included in the Orbilander concept (MacKenzie et al. 2021). How difficult these strategies would be to implement—landing a probe on the unknown terrain of Enceladus's surface or performing a large number of fly-throughs—is a discussion that is outside the scope of this study. However, we show that the sample sizes expected from both strategies would confidently sample at least one cell if we believe that most of the methane found in the plume comes from a population of methanogens (methane-informed case, or posterior). As a result, current mission and instrument design would be able to confidently reject the hypothesis that a monospecific methanogenic population is the source of the methane found by the Cassini Ion and Neutral Mass Spectrometer in the plume. However, these designs could miss the existence of a smaller population if the plume-found methane has an abiotic origin, in which case a larger sample is needed.

3.5. Bayesian Hypothesis Selection for Amino Acid Detection

Here we consider another potential biosignature that can be looked for in a sample of plume material: amino acid abundances (also examined in Steel et al. 2017; Guzman et al. 2019). Amino acids could be used as an important element for building a case for or against extraterrestrial life (Neveu et al. 2018). In ocean worlds such as Enceladus, amino acids could come from a primordial stock depending on the origin of the core material, but they are expected to degrade on geologically short timescales (Truong et al. 2019). Additionally, the decomposition kinetics are sufficiently slow that the concentration of amino acid is kept constant during the ocean plume's ascent that operates on a timescale of dozens of days (Steel et al. 2017; Truong et al. 2019). Together, these arguments make the case that probing the plume for amino acids could be of astrobiological significance. But amino acids can also be synthesized abiotically at significant concentrations, especially in hydrothermal settings (Shock & Schulte 1998), and as a consequence, detection alone cannot serve as an unambiguous biosignature. Strategies have been proposed to overcome this problem, including evaluating enantiomeric excess (Glavin et al. 2019) or homochirality (Chan et al. 2019, and references therein). Here we propose that because production rates, as well as the stoichiometric ratios of amino acids, differ depending on their biotic or abiotic origin, a Bayesian approach to biosignatures can be based on amino acid quantification (Amend et al. 2013; Moura et al. 2013; Steel et al. 2017).

We center our analysis on one of the most abundant amino acids: glycine (Gly). Glycine serves also as a reference from which estimates of concentrations of other amino acids can be derived using ratios in Steel et al. (2017) and Amend et al. (2013). According to Steel et al. (2017), abiotic production of amino acids in the hydrothermal vent could be $F_{aa} = 1.6\text{--}87 \text{ g s}^{-1}$, of which $f_{\text{Gly}} = 12\%$ is glycine. This production rate is

converted to a concentration in the HF:

$$[\text{Gly}]_{ab}^f = \frac{f_{\text{Gly}} F_{aa}}{M_{\text{Gly}} \int J_f}, \quad (37)$$

where $\int J_f$ is the total advection flux of HF (Affholder et al. 2021).

The proteic content of the Archean cell is poorly known, and its measurement is made difficult by the presence of the S-layer of glycoprotein in the cellular envelope. Therefore, in a first approximation, we assume that the putative methanogenic microorganisms contain the same relative abundances of amino acids as *Escherichia coli*. In *E. coli*, 50%–64% of cell dry mass is made of amino acids depending on the growth phase (Neidhardt 1996; Valgepea et al. 2013). Conservatively, we assume the value of $f_{aa}^{\text{E. coli}} = 50\%$. Genome analysis of *Methanocaldococcus jannaschii*, a model methanogenic archaea (Jones et al. 1983), shows a glycine fraction $f_{\text{Gly}}^{\text{M. jannaschii}} = 6.3\%$ (Bult et al. 1996; Moura et al. 2013). As a reference, $f_{\text{Gly}}^{\text{E. coli}} = 7.3\% \text{--} 7.4\%$; see Table S2 in Moura et al. (2013). Mass fraction is then converted into concentration using the molecular mass of Gly $M_{\text{Gly}} = 75.062 \text{ g mol}^{-1}$ and multiplying by the simulated waste biomass B_d^* (Equation (27)). Concentrations in the plume for both abiotic and biotic+abiotic cases are then estimated using Equation (7) and multiplying by a dilution or concentration factor if applicable. Biotic glycine is expected to be present in protein polymers that could themselves serve as biosignatures. We assume that sample treatment or retrieval methods allow (or impose) the separation of these hypothetical proteins into free amino acids, and thus we focus on the concentration in free amino acids.

We compare two scenarios: (i) abiotic synthesis of amino acids (as parameterized in Steel et al. 2017), and (ii) abiotic synthesis plus biotic production using our model (Section 2.3). We then calculate the confidence in either of these scenarios that a hypothetical measure of glycine concentration in the ocean plume would yield. In effect, this corresponds to the posterior probability calculated from Equation (29) for the competing models “abiotic” and “abiotic+biotic” (A and B in Equation (29)), given values of the glycine concentration in the ocean plume (x^0 in Equation (29)) and the prior probabilities of the models ($P(B) = 1 - P(A) = P(B|H)P(H)$, Equations (29) and (30)). Because the posterior probability is calculated assuming that either A or B is true ($P(A|x^0) = 1 - P(B|x^0)$), we do not calculate this probability when $P(x^0|B \cup A) < 0.05$; see Section 2.5.2. The calculations of $P(B|x^0) = f(x^0)$, $P(B)$ are shown in Figure 5. These calculations are done by first discarding constraints on hydrothermal vent composition and biotic methane production stemming from Cassini mission data (Figure 5(a), “prior” or “uninformed,” parameters drawn from distributions in Table 2) and then by leveraging the correlation between CH_4 (and H_2) abundance in the plume and biomass production in our model to further constrain biotic glycine production (Figure 5(b), “posterior” or “methane-informed”; Section 2.5). In the prior case, the prior probability $P(B)$ is bounded by the maximum value of $P(H) \approx 0.4$, which is the prior probability of habitability calculated in Affholder et al. (2021). In the posterior case, however, since the “habitable abiotic” and “biotic” (methane production) always match escape rates Φ_{H_2} and Φ_{CH_4} better than the “uninhabitable” model, the posterior values from Affholder et al. (2021), $P(B) \in [0, 1]$, are used. The maximum posterior value of $P(B)$ in Figure 3 of Affholder et al. (2021) is actually 0.95, but since

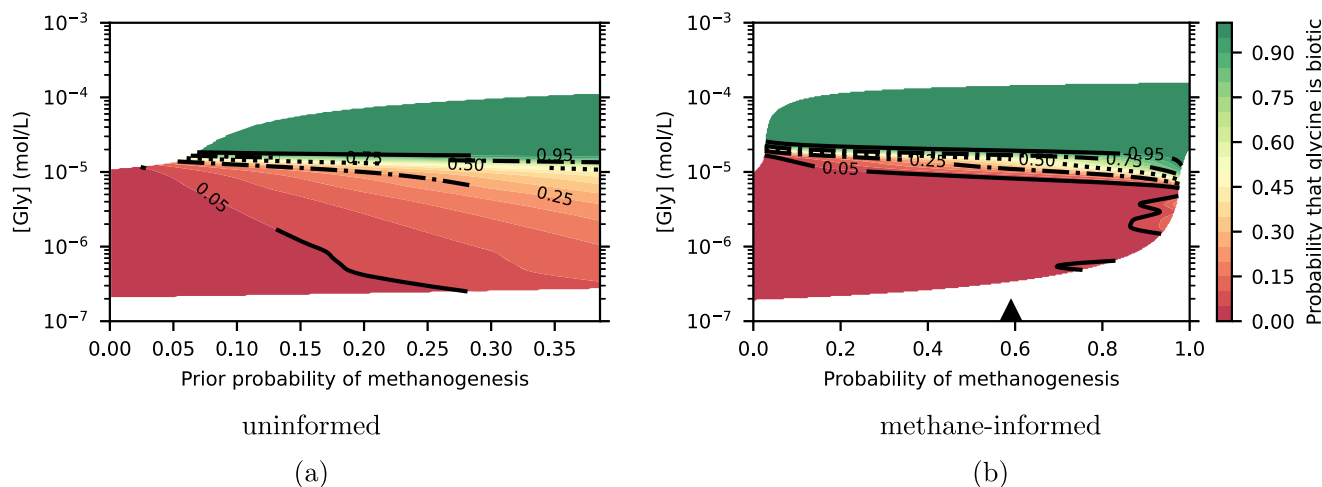


Figure 5. (a) Posterior confidence in biotic glycine production as a function of the observed glycine concentration in the ocean plume and the prior confidence in the existence of methanogens. The map is drawn only for glycine concentration values that fall in the 95% confidence interval of the total model (abiotic or abiotic + biotic). The prior probability of methanogenesis is here bounded by the prior probability of habitability (Section 2.5.1), hence the plot stopping at ≈ 0.4 . (b) Posterior (or methane-informed) confidence in biotic glycine production as a function of the observed glycine concentration and the prior confidence in the existence of methanogens using information from methane concentration in the plume. The black triangle denotes the average posterior probability of methanogenesis in Figure 3 of Affholder et al. (2021). This value highlights that a uniform prior distribution for $P(B|H)$ implies an average value of $E(P(B)) \approx 0.59$. In Affholder et al. (2021), the posterior probability of methanogenesis can reach unity (if the conditional probability of life emergence is also unity); therefore, the methane-informed case considers probability of methanogenesis up to 1.

this result is tied to the arbitrary upper bound on $[\text{CH}_4]_f$ (Figure 2 of Affholder et al. 2021 shows that with the upper bound of methane concentration in the HF taken from serpentinization experiments, the posterior $P(B)$ is 1), we allow ourselves to explore the prior space $P(B) \in [0, 1]$ when considering prospective inference based on glycine quantification in the ocean plume. Additionally, Figure 3 of Affholder et al. (2021) shows that assuming a uniform distribution $P(B|H) \sim U[0, 1]$ yields an average posterior $E(P(B)) \approx 0.59$. Even though the range in which $P(B|H)$ could be found is not known, it is worth noting that there is no reason a priori to consider the probability of methanogenesis in the methane-informed case as uniformly distributed in $[0, 1]$, as it might in fact be skewed to higher values than the unknown $P(B|H)$. To highlight this effect, we show the value of $E(P(B))_{P(B|H) \sim U[0,1]}$ on the horizontal axis of Figure 5(b).

As an example, if a future mission estimated that the concentration of glycine in the ocean plume were $[\text{Gly}] = 7 \times 10^{-6} \text{ mol L}^{-1}$, we would reject biotic production with high confidence under the assumption that life emergence is a rare event ($P(B) < 0.05$; Figure 5(a)). However, people convinced that life emergence is not rare could remain hopeful in that scenario, as the posterior probability of biotic glycine production remains relatively large for higher values of the prior $P(B)$ (about 0.25 for $P(B) = 0.35$ in the case of our hypothetical measure of $[\text{Gly}] = 7 \times 10^{-6} \text{ mol L}^{-1}$; Figure 5(a)). If we further impose the analysis of these hypothetical data to be consistent with data gathered by the Cassini mission (assuming that no abiotic source of methane matching these data better than methanogenesis would have been found), then even life emergence optimists would face a problem inferring biotic glycine production under this hypothetical measure, as a biosphere producing amounts of methane that match Cassini observations is unlikely to produce so little glycine in the ocean plume. The result would thus point toward the existence of an alternate source of methane working in addition to or in lieu of methanogenesis to explain plume-found methane levels.

There are cases for which the biotic hypothesis would be rejected regardless of the prior probability: if the glycine concentration is lower than $\approx 2 \times 10^{-7} \text{ mol L}^{-1}$, then the biotic model and the abiotic model are rejected (the likelihood of one or the other is less than 5%). In such a case, one would conclude that if a nonzero concentration is measured, the origin of glycine is likely not abiotic production in the hydrothermal setting as described in Amend et al. (2013) but another unknown pathway or possibly remains of a primordial stock if Enceladus's core is of carbonaceous chondrite or cometary origin. The so-called “methane-informed” case corresponds to the posterior estimates relative to volatile concentrations in the plume (methane in particular, denoted by “posterior” in Figures 1–4) and amounts to assuming that most of the plume-found methane is of biotic origin. In this case, we find that the abiotic production is favored when $[\text{Gly}] < 10^{-5} \text{ mol L}^{-1}$ (see Figure 5(b) and Table 4), regardless of the prior probability of methanogenesis. This second hypothesis (methane in the plume is biotic) is stronger than the “prior” case (methane in the plume could or could not be of biotic origin), and thus it is expected that it is easier to reject, given that it yields narrower predictions. Because the conditions of hypothesis rejection differ largely between the two cases (Table 4), investigation of methane sources potentially able to explain plume levels could help us in interpreting a hypothetical abundance of glycine. If a methane source concurrent to methanogenesis is identified, then our prior knowledge on a hypothetical biosphere is reduced. The interest of drawing such confidence maps (and the associated interpretation; see Table 4) is to help set the detection thresholds that should be aimed for in future in situ measurements, should a mission focus on amino acid detection and quantification.

The confidence maps in Figure 5 are calculated assuming that a hypothetical mission is able to accurately constrain the glycine concentration in the ocean plume based on a measure of the gas or ice or both phases in the space plume. For a reliable interpretation of a future result based on this analysis,

Table 4

Interpretation Key of Figure 5 in Terms of Hypothesis Selection and Rejection Based on the Observation of Glycine Concentration in the Ocean Plume

Range of Gly Concentration in the Ocean Plume	Biotic+Abiotic Gly Production	
	Uninformed/Prior	Methane-informed/Posterior
$>2 \times 10^{-5} \text{ mol L}^{-1}$	Favored	Favored
$2 \times 10^{-7} - 2 \times 10^{-5} \text{ mol L}^{-1}$	Not favored, but not rejected	Rejected
$<2 \times 10^{-7} \text{ mol L}^{-1}$	Rejected (with abiotic)	Rejected (with abiotic)

Note. Note that these ranges can be adjusted to account for biases in Gly concentration in material found in the space plume relative to the concentration in the ocean plume. For instance, if bubble scrubbing is expected to increase the concentration of Gly by a factor 1000 in the space plume, these ranges listed here can be multiplied by 1000.

one should correct the thresholds we propose in Table 4 by the estimated concentration or dilution factor between the bottom of the ice shell and the sampled plume. Main sources of dilution or concentration that could be evoked a priori are (i) plume dilution in the ocean, additional to the initial dilution of HF (e.g., Steel et al. 2017); (ii) alteration of organic molecules in the space plume due to exposure to ionizing radiation; (iii) organics concentration enhancement in the plume through bubble scrubbing (see Porco et al. 2017); and (iv) fractionation due to adsorption or condensation on ice walls of cracks in the shell (Spencer et al. 2018; Bouquet et al. 2019).

Our model neglects any dilution during the ocean plume ascent and structurally assumes a 1:3 ratio of HF to seawater (Section 2.1). This assumption is well supported by scaling laws derived for Europa's putative ocean plumes in Goodman et al. (2004), later replicated for Enceladus by Choblet et al. (2017), who show that the ocean plume is rotationally controlled until it reaches the ice shell. Steel et al. (2017) also reported an HF-to-seawater ratio of 1:10 in the ocean plume using 2D circulation numerical simulations. More recent studies on circulation in Enceladus's ocean, although not necessarily focused on ocean plume motion, do not appear to contradict these assumptions (Liao et al. 2020; Lobo et al. 2021; Zeng & Jansen 2021).

Ionizing radiation is unlikely to have a significant direct impact on the concentrations of organic molecules in the space plume. Transport time of ice grains in the plume before potential sampling altitudes or deposition is of the order of minutes to tens of minutes (assuming 1–10 μm diameter grains and a 65° ejection angle; Degruyter & Manga 2011). Once deposited on the surface of Enceladus, ice grains are expected to be buried faster than they would be altered under the harsher conditions of Europa's surface (Nordheim et al. 2018; Southworth et al. 2019). It is not known, however, whether the exposure times expected for ice grains from Enceladus's space plume allow free radicals to build up and oxidize organic molecules (Pasek 2020). Together, these arguments suggest that the influence of ionizing radiation on the concentration of organics in the material that could be sampled by a future mission might be reasonably neglected, be it fresh grains collected during a plume fly-through or deposited particles on the shallow subsurface.

The process of bubble scrubbing, or scavenging, is reviewed in Walls et al. (2014), and the possibility of this process for Enceladus's ocean outgassing is thoroughly discussed in Porco et al. (2017). Moreover, Postberg et al. (2018) have reported concentrated organic macromolecules being present in Enceladus's plume's ice grains, suggesting that bubble scrubbing occurs at the outgassing of oceanic matter to form the plume. It

has to be noted, however, that bubble scrubbing principally concerns macromolecules or whole cells, but it is unknown whether small organic molecules such as glycine are significantly affected by this process. On the other hand, volatile organic compounds might be adsorbed onto the ice walls or the ice grains during the outgassing of oceanic material.

Bouquet et al. (2019) show that organic compounds with a lower energy of desorption (e.g., ethylene, methanol, or formaldehyde) are not significantly affected by adsorption onto ice, whereas compounds with a desorption energy greater than approximately 0.7 eV are likely to be overrepresented on the surface of ice grains or to be retained on ice walls during outgassing. The desorption energy of glycine is not well constrained but could be ≈ 0.81 eV, and thus it could be significantly affected by adsorption onto ice (Escamilla-Roa & Moreno 2013; Bouquet et al. 2019). The abundance of adsorption sites on the ice wall surface is finite, and Bouquet et al. (2019) show that in relatively short timescales (tens of seconds) maximum coverage of the ice walls is reached. It is possible that water vapor condensation on the ice walls and subsequent freezing effectively prevent reaching that steady state (Spencer et al. 2018). However, Bouquet et al. (2019) review experimental work on the matter and conclude that condensation is unlikely to alter the composition of the gas phase, as adsorption is reversible and an ice wall equilibrium is still reached, even if water vapor condenses. Once this steady state is reached, the composition of the gas+ice phases should accurately reflect the composition of the ocean plume source material. If only the solid phase (ice grains) is to be considered, adsorption of glycine could result in overestimating its concentration in the source liquid phase. Whether adsorption of glycine could result in a significant depletion in the gas phase is unknown and depends on the relative velocities of the grains and the ice phase; modeling work extending the findings of Bouquet et al. (2019) is warranted to understand which phase (gas or ice grains) should be sampled to infer ocean composition. Finally, Pasek (2020) shows that during droplet freezing and sublimation ice grains lose about 20% of their water mass, hence slightly concentrating solutes. In conclusion, even though uncertainties remain on the effect of adsorption and bubble scrubbing on glycine, the concentrations predicted in the ocean plume in Figure 5 and Table 4 might be relatively conservative estimates of the concentrations in the plume material, especially if the gas and ice phases are sampled in adequate proportions.

Thus, we argue that a glycine-detection mission should aim for a minimal detection capability of $\approx 1 \times 10^{-7} \text{ mol L}^{-1}$. Mitić et al. (2009) report on a kinetic spectrophotometry method with

a theoretical detection limit just below this threshold ($6.5 \text{ ng mL}^{-1} \approx 8.7 \times 10^{-8} \text{ mol L}^{-1}$). (Whether this type of instrument could be used in situ or, on the contrary, whether a sample return would be necessary is outside the scope of this study.) In addition, other amino acid detection methods applicable to in situ characterization of Enceladus's plume exist and could meet the detection threshold that we calculated. Laser-induced fluorescence making use of a capillary electrophoresis microfluidic suite could reach the 1–100 picomolar limit of detection, well below our proposed threshold (Skelley et al. 2005; Creamer et al. 2017; Mathies et al. 2017; Casto-Bogges et al. 2021). Alternatively, mass-spectrometry-based methods of detection and analysis might also reach our proposed threshold (Ligterink et al. 2020). To conclude, while it might be hard to interpret a measure of $[\text{Gly}] > 2 \times 10^{-7} \text{ mol L}^{-1}$ unless organics enhancement (such as bubble scrubbing) can be confidently constrained, it seems quite feasible to reach sufficiently high detection capability (less than $2 \times 10^{-7} \text{ mol L}^{-1}$) for which the probability of false negatives is low. Thus, an amino acid detection strategy could yield significant scientific value, even if only glycine is studied. The inclusion of other amino acids in our framework could dramatically increase the capacity of our analysis to distinguish between abiotic and biotic sources, as different amino acids may be characterized by different relative abundances between biotic and abiotic origins (Amend et al. 2013; Creamer et al. 2017; Steel et al. 2017).

4. Conclusions and Implications for Future Missions

By using a detailed model of a putative population of methanogens in Enceladus's ocean, we found that the size of this hypothetical biosphere could be very small compared to previous estimates and to the size of Earth's hydrothermal vent biosphere. Nonetheless, we found that the cell density in the ocean plume could reach relatively high values (up to $10^7 \text{ cells mL}^{-1}$) if the biosphere is concentrated at the hydrothermal vent, rather than homogeneously distributed in the global ocean.

Although our predictions of cell density in the ocean plume are more often than not above detectable levels, a number of processes could affect the density of cells in the space plume material relative to cell density in the ocean plume. First, a significant amount of cells ejected in the plume could be destroyed owing to depressurization (Bywaters et al. 2020 report a potential cell destruction rate of 94% in depressurization experiments). Due to the linear relation between the concentration factor and the required sample volume shown in Figure 4, such an approximately 10-fold decrease in the intact cell abundance in the plume translates into an approximately 10-fold increase in the required minimal sample volume to about 1 mL compared to the case where abundance of cells in the plume directly reflects cell abundance in the ocean plume above the hydrothermal vent.

Second, cell-like abiotic structures (abiotic biomorphs) that may form in hydrothermal environments could cause a high risk of a false positive (Criouet et al. 2021). Assuming that cells can be identified unambiguously (see Nadeau et al. 2016), we find that the volume of plume material that needs to be collected to confidently sample at least one cell might require a large number of fly-throughs in the plume, or using a lander to collect plume particles falling on Enceladus's surface (e.g., the Enceladus Orbilander; MacKenzie et al. 2021).

Additionally, we show that aiming for the quantification of hypothetical amino acids could contribute a great deal to mount evidence for or against the hypothesis of an Earth-like methanogenic biosphere living in Enceladus's deep ocean using potentially smaller sample sizes. Although positive evidence is hard to achieve so long as there is uncertainty in abiotic processes, glycine abundance consistent with biotic production could then be combined with analysis of its abundance relative to other amino acids.

But considering the possibility of negative evidence should not be neglected. We found that a sufficiently capable instrument (with a lower detection threshold $\approx 10^{-7} \text{ mol L}^{-1}$) could help in challenging the hypothesis of Earth-like biotic processes taking place in Enceladus's ocean. As a result of the detection of sufficiently little or no glycine, this hypothesis would have to change into a more complex one and be tested against a different observable.

Lastly, our model considers a mono-metabolic, chemoautotrophic ecosystem, as do most estimates of cell density and biomass in Enceladus's ocean. Microbial ecosystems on Earth usually contain more than one species and contain both primary producers and heterotrophic consumers. Whether the presence of heterotrophs in Enceladus's ocean would significantly affect estimates of cell density and of the concentration of organic molecules exiting the local environment is not known. We believe that the ecological modeling approach used here provides an important first step in modeling a more complex ecosystem that would include heterotrophs. Such future work will accomplish the explicit and rigorous coupling of methanogenic primary production and anaerobic fermentation.

No current evidence points toward Enceladus's ocean being uninhabitable, or even uninhabited by Earth-like life. But a mission that would have the capacity to challenge this hypothesis could yield valuable science even in the event of negative results. Mission concepts currently under consideration suggest that such a mission is not beyond reach in the near future.

Appendix A

Scale-free Properties of the Physical Model

A.1. Abiotic Quantities Are Insensitive to Any Scale Parameter

The ML model presented in this article has some scale-free properties that arise from the parameterization of the flux of HF into the ML J_f . The shape parameters of the function $J_f(u)$ ensure that the total dissipated flux is equal to a particular value F and that the center of the ML is composed of 100% HF. These assumptions alone suffice to prove that (i) the range of thermal and chemical conditions existing around the vent is always from 100% HF to 100% seawater and (ii) abiotic concentrations in the initial ocean plume are entirely determined by the concentrations and temperature of the HF and seawater. Rewriting Equation (7) for the HF-to-seawater mixing ratio x^* at steady state,

$$\begin{aligned} x_{\text{OP}}^* &= \frac{\int x^*(u) J_c(u) 2\pi u du}{\int J_c(u) 2\pi u du} \\ &= \frac{1}{3}, \end{aligned} \quad (\text{A1})$$

or equivalently $C_i^{\text{OP}} = (1/3)C_i^f + (2/3)C_i^o$, which is independent of any physical parameter such as ϵ or the power

dissipated by the vent, F . A consequence of the independence of abiotic concentrations from vent power F is that patchiness has no effect on the abiotic concentrations in the initial ocean plume. The range of chemical and thermal conditions existing around the plume is also unchanged since the parameterization of the function J_f ensures that $x^*(0) = 1$ and $x^*(\infty) = 0$.

Moreover, the total flux of any solute i coming out of the ML (equal to $\int J_c C_i$) scales linearly with dissipated power F . As a consequence, the flux of i coming out of the hydrothermal environment is the same for a single vent dissipating F W and for the sum of an arbitrary number n of weaker vents each dissipating F/n W.

A.2. Relevant Biological Quantities Are Also Scale Independent

Equation (18) shows that the expression of the biomass concentration at steady state follows

$$B^* = \frac{1}{\epsilon \rho q_{\text{cat}}} (J_f (C_f^{eD} - C_o^{eD}) + J_c (C_o^{eD} - C^*_{eD})), \quad (\text{A2})$$

where eD is the electron donor (H_2 for methanogenesis) and $Y_{eD} = -1$ as a convention. Keeping in mind that both J_f and J_c scale with $\sqrt{\epsilon}$, B^* thus scales with $1/\sqrt{\epsilon}$.

At the same time, using the expression of c in Equation (5), the typical volume scale of the ML follows

$$\pi c^2 \epsilon \propto \sqrt{\epsilon}, \quad (\text{A3})$$

so that the quantity of cells (or biomass) in the hydrothermal environment is not sensitive to the chosen vertical scale ϵ . This analytical intuition extends to all fluxes and concentrations in the initial ocean plume and is verified by numerical simulations. Like in the abiotic case, all biological absolute quantities (except concentrations) scale linearly with F , and thus, again, the sum of n vents is equivalent to a single n times more powerful vent.

Appendix B Dead Cell Entrainment

Here we expand Equations (24) and (25) to separate dead cells into two categories. Some of the dead cells remain attached, and some are entrained by the circulating fluid and may end up in the ocean plume and be ejected through the cracks. We assume that this entrainment occurs with a fixed rate (or probability) η . The concentration of the fixed dead cells N_{dfix} follows

$$\frac{dN_{\text{dfix}}}{dt} = Nd - N_{\text{dfix}}\eta, \quad (\text{B1})$$

and the concentration of free-floating dead cells N_{dent} follows

$$\frac{dN_{\text{dent}}}{dt} = N_{\text{dfix}}\eta - \frac{J_c}{\rho\epsilon} N_{\text{dent}}. \quad (\text{B2})$$

At the steady state,

$$N_{\text{dfix}}^* = N^* \frac{d}{\eta}. \quad (\text{B3})$$

Thus,

$$N_{\text{dent}}^* = N^* \frac{\epsilon \rho d}{J_c}, \quad (\text{B4})$$

which is the same expression as in Equation (25), showing that the steady-state concentration of dead cells in the plume is insensitive to entrainment rate (but the total concentration of dead cells in the ML would adjust to be higher).

ORCID iDs

Antonin Affholder  <https://orcid.org/0000-0003-3481-0952>
 Boris Sauterey  <https://orcid.org/0000-0001-6164-756X>
 Régis Ferrière  <https://orcid.org/0000-0002-5806-5566>
 Stéphane Mazevet  <https://orcid.org/0000-0003-3557-6256>

References

- Affholder, A., Guyot, F., Sauterey, B., Ferrière, R., & Mazevet, S. 2021, *NatAs*, 5, 805
- Amend, J. P., LaRowe, D. E., McCollom, T. M., & Shock, E. L. 2013, *RSPTB*, 368, 20120255
- Bach, W., & Edwards, K. J. 2003, *GeCoA*, 67, 3871
- Bedrossian, M., Lindensmith, C., & Nadeau, J. L. 2017, *AsBio*, 17, 913
- Bouquet, A., Glein, C. R., & Waite, J. H. 2019, *ApJ*, 873, 28
- Brazelton, W. J., Schrenk, M. O., Kelley, D. S., & Baross, J. A. 2006, *ApEnM*, 72, 6257
- Bult, C. J., White, O., Olsen, G. J., et al. 1996, *Sci*, 273, 1058
- Bywaters, K., Stoker, C. R., Batista Do Nascimento, N., & Lemke, L. 2020, *Life*, 10, 40
- Cable, M. L., Clark, K., Lunine, J. I., et al. 2016, in 2016 IEEE Aerospace Conf. (Piscataway, NJ: IEEE), 1
- Cable, M. L., Porco, C., Glein, C. R., et al. 2021, *PSJ*, 2, 132
- Casto-Boggess, L. D., Golozar, M., Butterworth, A. L., & Mathies, R. A. 2021, *AnaCh*, 94, 1240
- Chan, M. A., Hinman, N. W., Potter-McIntyre, S. L., et al. 2019, *AsBio*, 19, 1075
- Choblet, G., Tobie, G., Sotin, C., et al. 2017, *NatAs*, 1, 841
- Connolly, J. P., & Coffin, R. B. 1995, *EnEng*, 121, 682
- Creamer, J. S., Mora, M. F., & Willis, P. A. 2017, *AnaCh*, 89, 1329
- Criouet, I., Viennet, J. -C., Jacquemot, P., Jaber, M., & Bernard, S. 2021, *GChPL*, 16, 40
- Csilléry, K., Blum, M. G., Gaggiotti, O. E., & François, O. 2010, *Trends in Ecology & Evolution*, 25, 410
- Daniel, R., Peterson, M., Danson, M., et al. 2010, *Biochemical journal*, 425, 353
- Degruyter, W., & Manga, M. 2011, *GeoRL*, 38, L16201
- DeMoll, E. 1993, in *Methanogenesis* (Chapman & Hall Microbiology Series) ed. J. G. Ferry (Berlin: Springer), 473
- Eigenbrode, J., Gold, R. E., McKay, C. P., Hurford, T., & Davila, A. 2018, *COSPAR*, 42, F3.6-3-18
- Escamilla-Roa, E., & Moreno, F. 2013, *P&SS*, 75, 1
- Glavin, D. P., Burton, A. S., Elsila, J. E., Aponte, J. C., & Dworkin, J. P. 2019, *ChRv*, 120, 4660
- Glein, C. R., Baross, J. A., & Waite, J. H. 2015, *GeCoA*, 162, 202
- Goodman, J. C., Collins, G. C., Marshall, J., & Pierrehumbert, R. T. 2004, *JGRE*, 109, E03008
- Goodman, J. C., & Lenferink, E. 2012, *Icar*, 221, 970
- Guzman, M., Lorenz, R., Hurley, D., et al. 2019, *IJASB*, 18, 47
- Hao, J., Glein, C. R., Huang, F., et al. 2022, *PNAS*, 119, e2201388119
- Hedderich, R., & Whitman, W. B. 2013, in *The Prokaryotes: Prokaryotic Physiology and Biochemistry*, ed. E. Rosenberg et al. (Berlin: Springer), 635
- Higgins, P., & Cockell, C. 2020, *Journal of the Royal Society Interface*, 17, 20200588
- Hoehler, T. M. 2004, *Geobiology*, 2, 205
- Hoehler, T. M. 2022, *NatAs*, 6, 3
- Hsu, H. -W., Postberg, F., Sekine, Y., et al. 2015, *Natur*, 519, 207
- Iess, L., Stevenson, D. J., Parisi, M., et al. 2014, *Sci*, 344, 78
- Jannasch, H. W., & Mottl, M. J. 1985, *Sci*, 229, 717
- Jones, W. J., Leigh, J. A., Mayer, F., Woese, C. R., & Wolfe, R. S. 1983, *Archives of Microbiology*, 136, 254
- Kelley, D. S., Karson, J. A., Fruh-Green, G. L., et al. 2005, *Sci*, 307, 1428
- Kleerebezem, R. O. B. E. R. T., & Van Loosdrecht, M. A. R. K. C. M. 2010, *Critical Reviews in Environmental Science and Technology*, 40, 1
- Liao, Y., Nimmo, F., & Neufeld, J. A. 2020, *JGRE*, 125, e06209
- Ligterink, N. F., Grimaudo, V., Moreno-García, P., et al. 2020, *NatSR*, 10, 1

- Lobo, A. H., Thompson, A. F., Vance, S. D., & Tharimena, S. 2021, *NatGe*, **14**, 185
- Lowell, R. P. 2017, *GeoRL*, **44**, 2703
- MacKenzie, S. M., Neveu, M., Davila, A. F., et al. 2021, *PSI*, **2**, 77
- Mathies, R. A., Razu, M. E., Kim, J., et al. 2017, *AsBio*, **17**, 902
- McCollom, T. M. 2000, *DSRI*, **47**, 85
- McCollom, T. M. 2016, *PNAS*, **113**, 13965
- McCollom, T. M., & Donaldson, C. 2016, *AsBio*, **16**, 389
- Menden-Deuer, S., & Lessard, E. J. 2000, *LimOc*, **45**, 569
- Mitić, S. S., Pavlović, A. N., Tošić, S. B., Arsić, B. B., & Sunarić, S. M. 2009, *AnaCh*, **64**, 683
- Moura, A., Savageau, M. A., Alves, R., & Ouzounis, C. A. 2013, *PLoSO*, **8**, e77319
- Nadeau, J., Lindensmith, C., Deming, J. W., Fernandez, V. I., & Stocker, R. 2016, *AsBio*, **16**, 755
- Neidhardt, F. C. 1996, *Cellular and Molecular Biology*, **1**, 1225
- Neveu, M., Anbar, A. D., Davila, A. F., et al. 2020, *FrASS*, **7**, 26
- Neveu, M., Hays, L. E., Voytek, M. A., New, M. H., & Schulte, M. D. 2018, *AsBio*, **18**, 1375
- Nordheim, T. A., Hand, K. P., & Paranicas, C. 2018, *NatAs*, **2**, 673
- Orcutt, B. N., LaRowe, D. E., Biddle, J. F., et al. 2013, *Frontiers in Microbiology*, **4**, 189
- Oren, A. 2014, *The Prokaryotes-Other Major Lineages of Bacteria and the Archaea* (Berlin: Springer), 215
- Pasek, M. A. 2020, *FrASS*, **7**, 14
- Pershing, A. J., Christensen, L. B., Record, N. R., et al. 2010, *PLoSO*, **5**, e12444
- Porco, C. C., Dones, L., & Mitchell, C. 2017, *AsBio*, **17**, 876
- Postberg, F., Khawaja, N., Abel, B., et al. 2018, *Natur*, **558**, 564
- Ray, C., Glein, C. R., Waite, J. H., et al. 2021, *Icar*, **364**, 114248
- Sauterey, B., Chamay, B., Affholder, A., Mazevet, S., & Ferriere, R. 2020, *NatCo*, **11**, 1
- Schrenk, M. O., Kelley, D. S., Bolton, S. A., & Baross, J. A. 2004, *Environmental Microbiology*, **6**, 1086
- Shock, E. L., & Schulte, M. D. 1998, *JGR*, **103**, 28513
- Skelly, A. M., Scherer, J. R., Aubrey, A. D., et al. 2005, *PNAS*, **102**, 1041
- Southworth, B. S., Kempf, S., & Spitale, J. 2019, *Icar*, **319**, 33
- Spencer, J., Howett, C., Verbiscer, A., et al. 2013, EPSC, EPSC2013-840
- Spencer, J., Nimmo, F., Ingersoll, A. P., et al. 2018, in *Enceladus and the icy moons of Saturn*, ed. P. M. Schenk et al. (Tucson, AZ: Univ. Arizona Press), 163
- Steel, E. L., Davila, A., & McKay, C. P. 2017, *AsBio*, **17**, 862
- Taubner, R. -S., Pappenreiter, P., Zwicker, J., et al. 2018, *NatCo*, **9**, 748
- Thomas, P. C., Tajeddine, R., Tiscareno, M. S., et al. 2016, *Icar*, **264**, 37
- Tijhuis, L., Van Loosdrecht, M. C. M., & Heijnen, J. J. 1993, *Biotechnology and bioengineering*, **42**, 509
- Truong, N., Monroe, A. A., Glein, C. R., Anbar, A. D., & Lunine, J. I. 2019, *Icar*, **329**, 140
- Tsou, P., Brownlee, D. E., McKay, C. P., et al. 2012, *AsBio*, **12**, 730
- Valgepea, K., Adamberg, K., Seiman, A., & Vilu, R. 2013, *Molecular BioSystems*, **9**, 2344
- Virtanen, P., Gommers, R., Oliphant, T. E., et al. 2020, *NatMe*, **17**, 261
- Waite, J. H., Glein, C. R., Perryman, R. S., et al. 2017, *Sci*, **356**, 155
- Walls, P. L., Bird, J. C., & Bourouiba, L. 2014, *American Zoologist*, **54**, 1014
- Ward, B. A., Dutkiewicz, S., Jahn, O., & Follows, M. J. 2012, *LimOc*, **57**, 1877
- Wolin, M. 1976, in *Microbial Formation and Utilization of Gases*, ed. H.G. Schlegel et al. (Göttingen: Goltze KG), 141
- Zeng, Y., & Jansen, M. F. 2021, *PSI*, **2**, 151